Accelerated MRI Thermometry by Direct Estimation of Temperature from Undersampled k-Space Data

Pooja Gaur[1,2]* and William A. Grissom[1,3,4,5]

Purpose: Acceleration of magnetic resonance (MR) thermometry is desirable for several applications of MR-guided focused ultrasound, such as those requiring greater volume coverage, higher spatial resolution, or higher frame rates.
Methods: We propose and validate a constrained reconstruction method that estimates focal temperature changes directly from k-space without spatial or temporal regularization. A model comprising fully-sampled baseline images is fit to undersampled k-space data, which removes aliased temperature maps from the solution space. Reconstructed temperature maps are compared to maps reconstructed using parallel imaging (iterative self-consistent parallel imaging reconstruction [SPIRiT]) and conventional hybrid thermometry, and temporally constrained reconstruction thermometry.
Results: Temporal step response simulations demonstrate finer temporal resolution and lower error in 4×-undersampled radial k-space reconstructions compared to temporally constrained reconstruction. Simulations show that the k-space method can achieve higher accelerations with multiple receive coils. Phantom heating experiments further demonstrate the algorithm's advantage over reconstructions relying on parallel imaging alone to overcome undersampling artifacts. In vivo model error comparisons show the algorithm achieves low temperature error at higher acceleration factors (up to 32× with a radial trajectory) than compared reconstructions.
Conclusion: High acceleration factors can be achieved using the proposed temperature reconstruction algorithm, without sacrificing temporal resolution or accuracy. **Magn Reson Med 73:1914–1925, 2015. © 2014 Wiley Periodicals, Inc.**

Key words: temperature imaging; image reconstruction; non-Cartesian imaging; parallel imaging; high-intensity focused ultrasound; magnetic resonance imaging-guided focused ultrasound

[1]Institute of Imaging Science, Vanderbilt University, Nashville, Tennessee, USA.

[2]Department of Chemical and Physical Biology, Vanderbilt University, Nashville, Tennessee, USA.

[3]Department of Biomedical Engineering, Vanderbilt University, Nashville, Tennessee, USA.

[4]Department of Radiology, Vanderbilt University, Nashville, Tennessee, USA.

[5]Department of Electrical Engineering, Vanderbilt University, Nashville, Tennessee, USA.

*Correspondence to: Pooja Gaur; B.S., Vanderbilt University Institute of Imaging Science, 1161 21st Avenue South, Medical Center North, AA-1105 Nashville, TN 37232. E-mail: pooja.gaur@vanderbilt.edu

INTRODUCTION

Recent technological developments have combined thermal therapies with magnetic resonance imaging (MRI) for targeting, temperature monitoring and assessment of thermal dose in the brain and body (1). In particular, MRI-guided focused ultrasound (MRgFUS) is increasingly being applied to treat uterine fibroids and cancer (2–5), relieve pain from bone metastases (6,7), and stimulate deep brain tissue to treat neurological conditions (8,9). Additionally, animal studies have demonstrated that MRgFUS can induce gene expression (10) and also facilitate drug delivery (11), even across the blood-brain barrier (12,13).

In MRgFUS, ultrasound energy is generated outside the body and delivered noninvasively to a specific location within the tissue, ideally without affecting any tissues outside the targeted volume. The primary role of MRI in the procedures is to provide images with soft tissue contrast for targeting, and to provide real-time temperature measurements to monitor thermal dose to the targeted tissue, where temperature measurements are conventionally based on the proton resonance frequency (PRF) shift with temperature. Although acoustic energy is nominally focused to a single point in the body, there is an ever-present risk that dangerous heating may occur in other regions in the near- and far-fields of the transducer, so it is desirable to measure temperature rises with as high a frame rate as possible throughout the tissue to ensure patient safety. However, MRgFUS procedures are currently limited to two-dimensional temperature imaging of a handful of slices in real-time. For example, typical thermometry protocols for closed-loop ablation of uterine fibroids use spoiled gradient echo or multishot echo-planar imaging (EPI) to image up to six slices (14,15) approximately every 3 s. However, due to their limited volume coverage those scans can miss dangerous heating that can occur outside the target volume, particularly near tissue interfaces and bones (16). Some form of scan acceleration is required to simultaneously achieve large volume coverage and a high frame rate in thermometry, using either pulse sequences that acquire k-space data faster (17) or temperature reconstructions that do not require full k-space data.

Temperature reconstruction-based approaches to accelerating magnetic resonance (MR) thermometry can be loosely grouped into three categories: parallel imaging, compressed sensing, and temporal regularization-based approaches. Parallel imaging with multiple receive coils is commonly used to accelerate anatomical and functional MR imaging (18,19), and has been applied to thermometry (20–24). However, to achieve high accelerations, parallel imaging requires many coils in close proximity with the body, which is often impossible in MRgFUS as the FUS apparatus is large and must be in direct contact with the body.

Because of these limitations, the development of MRgFUS-compatible coil arrays is an active area of research, and state-of-the-art arrays still comprise many fewer coils than are typically used in conventional parallel imaging (25–27).

Compressed sensing (28) has also been applied to MR thermometry (29,30). However, these techniques rely on compressibility of image magnitude to constrain the solution space, and errors can arise when the phase component of the image contains high spatial frequency variations such as those caused by heating (31). Furthermore, compressed sensing must typically be combined with parallel imaging to achieve high accelerations. Compressed sensing reconstructions that incorporate phase regularization have been proposed for thermometry (31,32), but to date no such method has been described that robustly enables high acceleration factors in a wide variety of acquisition scenarios.

Temporal regularization-based approaches (24,33–35) assume that images or temperature change slowly during treatment. For example, the temporally constrained reconstruction (TCR) method (33) jointly reconstructs treatment images using a temporal roughness penalty. This enables acceleration when the k-space undersampling pattern is alternated in time so that aliasing artifacts move between consecutive images and are filtered out by the penalty. Other temporal regularization-based approaches have leveraged the bioheat equation and/or Kalman filtering, either to similarly suppress rapidly changing aliasing artifacts while preserving slower temperature changes, or to interpolate between fully sampled temperature images acquired at a lower frame rate (34,35). Although all these approaches are capable of producing temperature maps at any desired frame rate, due to regularization their true temporal resolution lies somewhere between the accelerated and fully-sampled frame rates. Furthermore, the alternating k-space sampling patterns required by some methods may lead to increased eddy current distortions, and generally limit pulse sequence design.

This work introduces an approach to accelerated temperature imaging that is based on fitting a constrained treatment image model directly to undersampled k-space data. Because the treatment image model comprises fully-sampled pretreatment/baseline images, aliased temperature maps are removed from the solution space, without temporal regularization. The method is compatible with parallel imaging and can be used with any readout trajectory. Simulations will demonstrate improvements in temporal resolution compared to TCR, that the method is compatible with and benefits from multicoil receive, and that it is robust to motion and rapidly varying background anatomical phase. Experiments will investigate in vivo model error as a function of acceleration, and compare the method to conventional parallel imaging reconstructions. Aspects of this work have been previously reported elsewhere (36,37).

THEORY

Signal Model and Problem Formulation

The proposed method estimates temperature maps from undersampled k-space data by fitting a constrained image model directly to the data, without an explicit image reconstruction step. The hybrid multibaseline and referenceless treatment image model is used (38), which comprises a weighted combination of fully-sampled baseline images acquired prior to heating, a polynomial phase shift to model center frequency drift and other bulk phase shifts unrelated to heating, and a spatially-sparse heating-induced phase shift. When applied to estimate temperature maps from fully-sampled images, hybrid thermometry has been shown to produce accurate temperature measurements in the human brain and porcine liver with FUS heating (39,40), and in the human heart and liver with motion (38).

The k-space signal model is the discrete Fourier transform (DFT) of the hybrid image model:

$$y_i = \sum_{j=1}^{N_s} e^{i\vec{k}_i \cdot \vec{x}_j} \left(\sum_{l=1}^{N_b} b_{l,j} w_l \right) e^{i\left(\{Ac\}_j + \theta_j \right)} + \varepsilon_i, \qquad [1]$$

where y_i is one k-space data sample, $i = 1, \ldots, N_k$ indexes the N_k acquired samples, N_s is the number of image voxels, $\vec{k}_i$ is the k-space location of sample i, the $\{\boldsymbol{b}_l\}_{l=1}^{N_b}$ are complex baseline library images reconstructed from fully sampled k-space data acquired prior to treatment, the w_l are baseline image weights, $\boldsymbol{A}$ is a matrix of smooth (e.g., low-order polynomial) basis functions, $\boldsymbol{c}$ is a polynomial coefficient vector, $\boldsymbol{\theta}$ is a heating-induced phase shift, which is negative for a temperature increase (41) and is assumed to contain mostly zero entries, and ε is complex Gaussian noise. The role of the baseline library images $\{\boldsymbol{b}_l\}_{l=1}^{N_b}$ is to capture physiological and anatomical amplitude and phase variations across respiratory and cardiac cycles. The role of the polynomial phase shift $\boldsymbol{Ac}$ is to model phase changes induced by smooth magnetic field shifts, such as center frequency drift and those caused by respiration and bowel filling. The phase shift $\boldsymbol{\theta}$ that results from targeted heating is modeled as a focal shift separate from these other phase components. Sparsity of $\boldsymbol{\theta}$ is exploited by the algorithm to separate it from the polynomial phase shift, and reflects the fact that in a targeted thermal therapy like MRgFUS, temperature rises will occur in a minority of image voxels. To estimate $\boldsymbol{\theta}$, the signal model in Eq. [1] is fit to acquired k-space data $\tilde{\boldsymbol{y}}$ by solving the constrained minimization problem:

$$
\begin{aligned}
\text{minimize} \quad & \frac{1}{2} \left\| \tilde{\boldsymbol{y}} - \boldsymbol{y}(\boldsymbol{w}, \boldsymbol{c}, \boldsymbol{\theta}) \right\|^2 + \lambda \|\boldsymbol{\theta}\|_1, \\
\text{subject to} \quad & \boldsymbol{\theta} \leqslant 0 \\
& \sum_{l=1}^{N_b} w_l = 1 \qquad\qquad [2] \\
& \boldsymbol{w} \geqslant 0,
\end{aligned}
$$

where the first term in the objective function is proportional to the negative log-likelihood of the data (when neglecting noise in the baseline images), $\|\boldsymbol{\theta}\|_1$ is the ℓ_1 norm of $\boldsymbol{\theta}$, and λ is a regularization parameter that controls the sparsity of $\boldsymbol{\theta}$.

This method can reconstruct artifact-free temperature maps from undersampled k-space data because the fully-sampled baseline image component of the model removes images (and corresponding temperature maps) from the solution space that contains aliasing artifacts in their magnitude. Solutions containing aliasing artifacts in their phase that cannot be modeled by some combination of the baseline images, a polynomial phase shift, and a sparse phase shift are also eliminated from the solution space.

Algorithm

A solution to the problem in Eq. [2] is found using the following alternating minimization algorithm, given initial estimates of w, c, and θ:

1. **repeat**
2. Update w: A quadratic programming problem,

$$\text{minimize} \quad \frac{1}{2}\left\| \tilde{y} - G\text{diag}\left\{e^{\imath(\{Ac\}_j + \theta_j)}\right\}Bw \right\|^2$$

$$\text{subject to} \quad \sum_{l=1}^{N_b} w_l = 1 \qquad [3]$$

$$w \geqslant 0,$$

   is solved, where G is a (possibly nonuniform) DFT matrix, and B is a matrix whose columns are the baseline images.

3. Update θ: The following constrained minimization problem is solved using the nonlinear conjugate gradient algorithm described in Appendix (42):

$$\text{minimize} \quad \frac{1}{2}\left\| \tilde{y} - G\text{diag}\left\{e^{\imath\theta_j}\right\}f \right\|^2 - \lambda\sum_{j=1}^{N_s}\theta_j \qquad [4]$$

$$\text{subject to} \quad \theta \leqslant 0,$$

   where $f_j \triangleq e^{\imath\{Ac\}_j}\{Bw\}_j$.

4. Update c: The update for c is similar to the θ update, except that the gradient, and consequently the nonlinear conjugate gradient search direction, incorporate the basis matrix A,

$$\nabla_c\Psi = A'\nabla_\theta\Psi, \qquad [5]$$

   and there are no nonpositivity constraints.

5. **until** Stopping criterion met
6. To eliminate temperature bias due to the ℓ_1 norm, steps 1–5 are repeated with $\lambda = 0$, and θ is only updated in voxel locations that were more negative than a threshold value after step 5.

Parallel Imaging

When imaging with more than one receive coil, (w, c, θ) are simultaneously fit to all coils' data. Because the baseline images are weighted by the coil sensitivities, the algorithm implicitly performs a SENSE reconstruction (18,43), without requiring a separate sensitivity map measurement. It will be demonstrated in simulations that the algorithm is able to exploit multiple receive coils to improve temperature map accuracy at higher accelerations, compared to a single receive coil.

METHODS

Algorithm Implementation

The proposed algorithm was implemented in MATLAB R2013a (Mathworks, Natick, MA) on a workstation with a 3.4 GHz E31270 Intel Xeon CPU (Intel Corporation, Santa Clara, CA) and 16 GB of RAM.[1] The DFT matrix G was evaluated using nonuniform fast Fourier transforms (44). Baseline images were reconstructed from fully-sampled k-space data using a conjugate gradient (CG) algorithm (45). When more than one baseline image was used, the baseline image weights w were solved for using MATLAB's quadprog function. The polynomial phase coefficient vector c and temperature phase shift vector θ were initialized to zeros. Updates for c and θ used five iterations. Voxels where θ was more negative than -0.01 radians were corrected for temperature bias due to the ℓ_1 norm as described in step 6 of the algorithm. In this stage, c and θ updates contained 5 and 10 iterations, respectively. The algorithm stopped when the relative change in the objective function was less than 0.1% between consecutive iterations.

In the following simulations and experiments, the k-space thermometry algorithm is compared with TCR (33) and temperature maps estimated after image reconstruction by either CG or iterative self-consistent parallel imaging reconstruction (SPIRiT) (46), using a hybrid thermometry image model. SPIRiT kernels were calibrated using the (fully-sampled) baseline image and reconstructions used a 5×5 kernel and a 30×30 calibration region, and the SPIRiT regularization parameter was set to the median of the absolute value of the k-space data. Given a reconstructed image m from CG or SPIRiT, temperature phase shifts were estimated as:

$$\theta_j = \angle(m_j f_j^*), \qquad [6]$$

for each voxel j, where f is the baseline image with polynomial phase shift estimated by the k-space algorithm.

Temporal Step Response Simulation

To investigate the temporal step response of reconstructed temperature maps and compare it to TCR, k-space data of a simulated circular phantom and an instantaneous on-off Gaussian-shaped (full width at half maximum [FWHM] of 0.8 pixels) heat-induced phase shift were generated for a golden angle (GA) radial trajectory with field of view (FOV) = 20 cm, matrix size = 64×64, echo time (TE) = 16 ms, and 101 radial lines for full sampling. The peak phase shift of 1.7 radians corresponded to 13°C heating at 3 T. The median absolute value of the k-space data was 4.37. Temperature change maps were reconstructed at 4× acceleration (25 lines, 91 samples per line) using TCR and the k-space method. TCR reconstructions used a weighting factor α = 100 and 100 iterations. The k-space method used λ = 10^{-4}, one baseline image, and a zeroth-order polynomial fit.

Multicoil Receive Simulation

The same circular object and Gaussian-shaped phase shift were generated with the same settings as the temporal step response simulation for a single receive coil with uniform sensitivity, and for a simulated 8-channel 3 T receive coil array (47). k-Space data were synthesized using GA radial and 2DFT readout trajectories. Temperature maps were reconstructed by the k-space method and by Eq. [6] from images reconstructed by SPIRiT from the 8-channel data. Reconstructions were performed across a range of acceleration factors, with 64 (2DFT) and 91 (GA radial) k-space samples per line. The k-space method again used $\lambda = 10^{-4}$, one baseline image, and a zeroth-order polynomial fit.

Motion Simulation

A simulation was performed to validate the algorithm's robustness to motion and its ability to regress rapidly varying background anatomical phase, in the same manner as was done in Ref. 38 for the image-domain hybrid algorithm. 64×64 images of a rectangular object were generated with background phase comprising a weighted sum of low-frequency Fourier components. A library of 50 baseline images was generated across a range of vertical organ positions, representative of motion that could be observed in the liver as part of a normal breathing cycle. One hundred uniformly-distributed random positions within this range were chosen and used to synthesize treatment images with Gaussian-shaped phase shifts to simulate focal heating (peak magnitude corresponding to a 23°C heat rise at 3 T) and sixth-order random polynomial phase shifts. k-Space data were generated from the treatment images using an 8×-accelerated radial trajectory (12 lines, 91 samples per line) with one receive coil and FOV = 20 cm, matrix size = 64×64, and TE = 16 ms. The k-space temperature reconstruction algorithm was applied using the generated baseline library, a sixth-order polynomial fit, and $\lambda = 0.2$. A second-order finite differencing spatial roughness penalty (with regularization parameter $\beta = 1$) was added to the $\boldsymbol{\theta}$ cost function following the method described in Ref. 48. The median k-space data amplitude was 0.75.

Phantom Heating Experiments

To evaluate the method model experimentally, a tissue-mimicking gel phantom was sonicated using a Philips Sonalleve MR-HIFU system (Philips Healthcare, Vantaa, Finland) operated at 1.2 MHz and 100 W for 36 s, and targeting a 12-mm diameter treatment cell. The system was installed on a 3 T scanner (Philips Achieva, Philips Healthcare, Best, The Netherlands). Gradient echo imaging was performed for temperature monitoring with 2DFT and GA radial readout trajectories and five receive coils. Parameters for the 2DFT and GA radial sequences were: FOV = 40 cm; matrix size = 192×192; slice thickness = 7 mm; pulse repetition time (TR) = 32 ms; TE = 16 ms. The multicoil data were compressed to three coils by thresholding the singular values of the data matrix at 5% of the largest singular value. The median k-space data amplitude was 8.58 for 2DFT and 15.65 for GA radial scans. In addition to the k-space domain reconstructions, temperature maps were estimated using Eq. [6] and images reconstructed by CG and SPIRiT. Temperature maps were reconstructed to a 96×96 matrix with 20-cm FOV. Reconstructions used one baseline image, a zeroth-order polynomial fit, $\lambda = 0.016$ (2DFT) and 0.0075 (GA radial), and $\beta = 2^{-11}$ (2DFT) and 2^{-12} (GA radial). 2DFT reconstructions were performed after taking every fifth line of the original 192×192 matrix in either the *x*- or *y*-direction, corresponding to 2.5× acceleration relative to the 20-cm reconstructed FOV (39 lines; 96 samples per line after averaging adjacent samples in the original matrix). GA radial data were undersampled by 16× relative to the 20-cm reconstructed FOV (9 lines; 192 samples per line).

In Vivo Model Validation

To validate the k-space signal model in vivo in the absence of heat, sagittal brain images were collected in a healthy volunteer using an 8-channel receive array and GA radial readout trajectory at 3 T (Philips Achieva, Philips Healthcare, Best, The Netherlands) under approval of the Institutional Review Board at Vanderbilt University with: FOV = 25.6 cm; matrix size = 128×128; slice thickness = 3 mm; TR = 100 ms; TE = 10 ms; 256 k-space samples per line. Multicoil data were compressed to four coils using singular value thresholding as in the phantom heating experiments. Temperature maps were estimated using k-space reconstructions and Eq. [6] with CG- and SPIRiT-reconstructed images. To evaluate temperature errors that could arise in the k-space reconstructions, the algorithm was executed without the $\boldsymbol{\theta}$ updates (step 3 was skipped and $\boldsymbol{\theta}$ was fixed at 0) so that only the baseline image weights and background phase shift were estimated, using seven baseline images and a first-order polynomial matrix. Then, keeping those baseline image and polynomial phase estimates fixed by skipping steps 2 and 4, the algorithm was repeated to fit $\boldsymbol{\theta}$ with $\lambda = 0$. Temperature maps were reconstructed with no acceleration (256 lines; 97 maps), 2× acceleration (128 lines; 109 maps), 4× acceleration (64 lines; 116 maps), 8× acceleration (32 lines; 119 maps), 16× acceleration (16 lines; 121 maps), and 32× acceleration (8 lines; 121 maps). Errors were averaged over dynamic frames to determine the mean errors for each acceleration factor. The median k-space data amplitude was 85.04.

RESULTS

Temporal Step Response Simulation

The fully-sampled and undersampled k-space trajectories and corresponding magnitude image and baseline subtraction temperature map reconstructions of the simulated data are shown in Figure 1a. Undersampling results in a noisy appearance of the magnitude image and coherent streaking artifacts in the temperature maps. The temperature in the center voxel is plotted for the true and reconstructed maps in Figure 1b. The k-space method better tracks the instantaneous temperature changes, achieving finer temporal resolution than TCR.
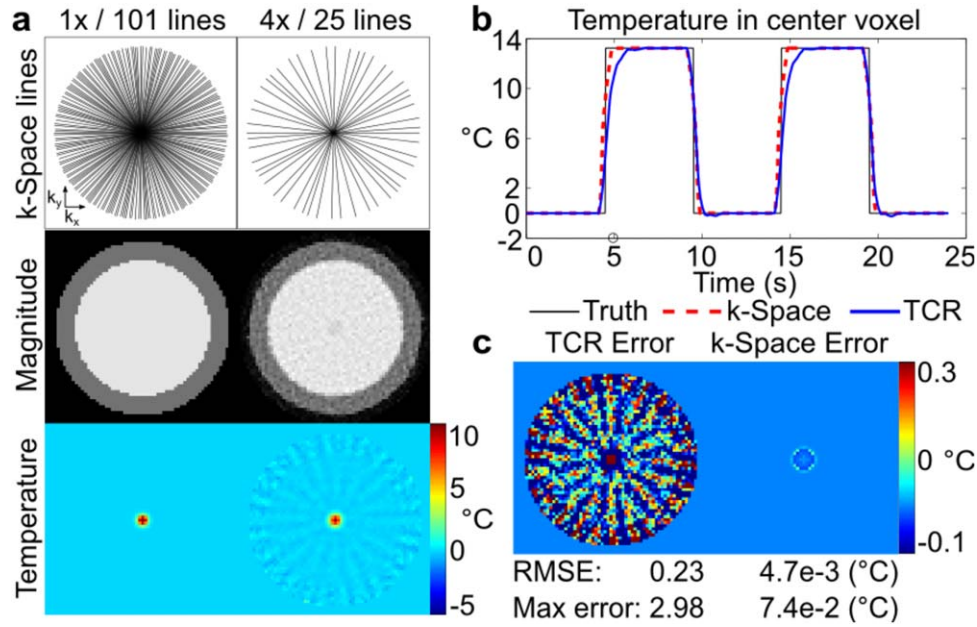
FIG. 1. Temporal step response simulation. **a**: Illustration of fully sampled and 4×-undersampled radial trajectories and corresponding image and baseline subtraction temperature map reconstructions. Undersampling results in noisy-looking magnitude images and streaking in temperature maps. **b**: Temperature in the center of the hot spot versus time. The proposed k-space-based reconstruction achieves finer temporal resolution than TCR as it does not depend on temporal regularization to suppress aliasing artifacts. **c**: Just after the step temperature rise at 5 s [circle on *x*-axis in (b)], aliasing artifacts are visible in the TCR estimate, but not in the k-space method's estimate.

Figure 1c shows temperature maps at 5 s, immediately after a transition. The k-space reconstruction has small truncation errors around the hot spot, but overall much lower error and no visible aliasing artifacts. With TCR, aliasing artifacts could be reduced by increasing temporal regularization, but this would further degrade temporal resolution.

Multicoil Receive Simulation

Multicoil receive simulation results are shown in Figure 2. Root-mean-square error within the object, maximum error within the object excluding the temperature hot spot, and error in the center voxel of the reconstructed temperature maps were calculated for the 2DFT and GA radial reconstructions. The changing interference of coherent aliases at different acceleration factors results in oscillation in the 2DFT SPIRiT errors. Similar patterns are observed to a lesser degree in the single-coil k-space reconstructions at higher acceleration factors. However, the multicoil k-space reconstructions are free from these artifacts and produce temperature estimates with low error using as few as four readout lines, indicating that the accuracy of the k-space method's reconstructions improves with multiple receive coils. GA radial reconstructions using the k-space-based method do not exhibit significant aliasing artifacts in either single-coil or multicoil cases. Error remains low for single-coil k-space estimates even when only two radial lines are used for temperature reconstruction. In contrast, the SPIRiT reconstructions are increasingly affected by undersampling artifacts with increasing acceleration factor.

Motion Simulation

Results from one of the object positions are shown in Figure 3. Figure 3f shows the residual phase after k-space thermometry, which was calculated by subtracting the fitted hybrid image model phase from the synthesized treatment image phase. No large residual phase errors are present within the object. The root-mean-square (RMS) and maximum temperature errors corresponding to the residual phase errors across all the random positions were 0.16 and 1.19°C, respectively. The temperature maps were also accurately estimated (Fig. 3g,h). The RMS and maximum temperature map errors were 0.10 and 1.47°C, respectively. These results indicate that the hybrid signal model was able to account for all sources of phase, and that the k-space thermometry algorithm was able to determine the parameters of that model.

Phantom Heating Experiments

Figure 4 shows the 2DFT phantom experiment results. Image-domain temperature reconstructions were highly sensitive to the relative orientation of the coil array (which encoded primarily along *x*) and the undersampled dimension, and aliasing artifacts in the images were lower when data were undersampled along the *x*-direction. Compared to the CG reconstruction, the SPIRiT algorithm was able to reduce but not fully remove artifacts from undersampling, likely due to the low number of receive channels (three, after coil compression) relative to the acceleration factor (2.5×). The k-space temperature reconstructions were free from artifacts, regardless of the undersampled dimension. Figure 4c
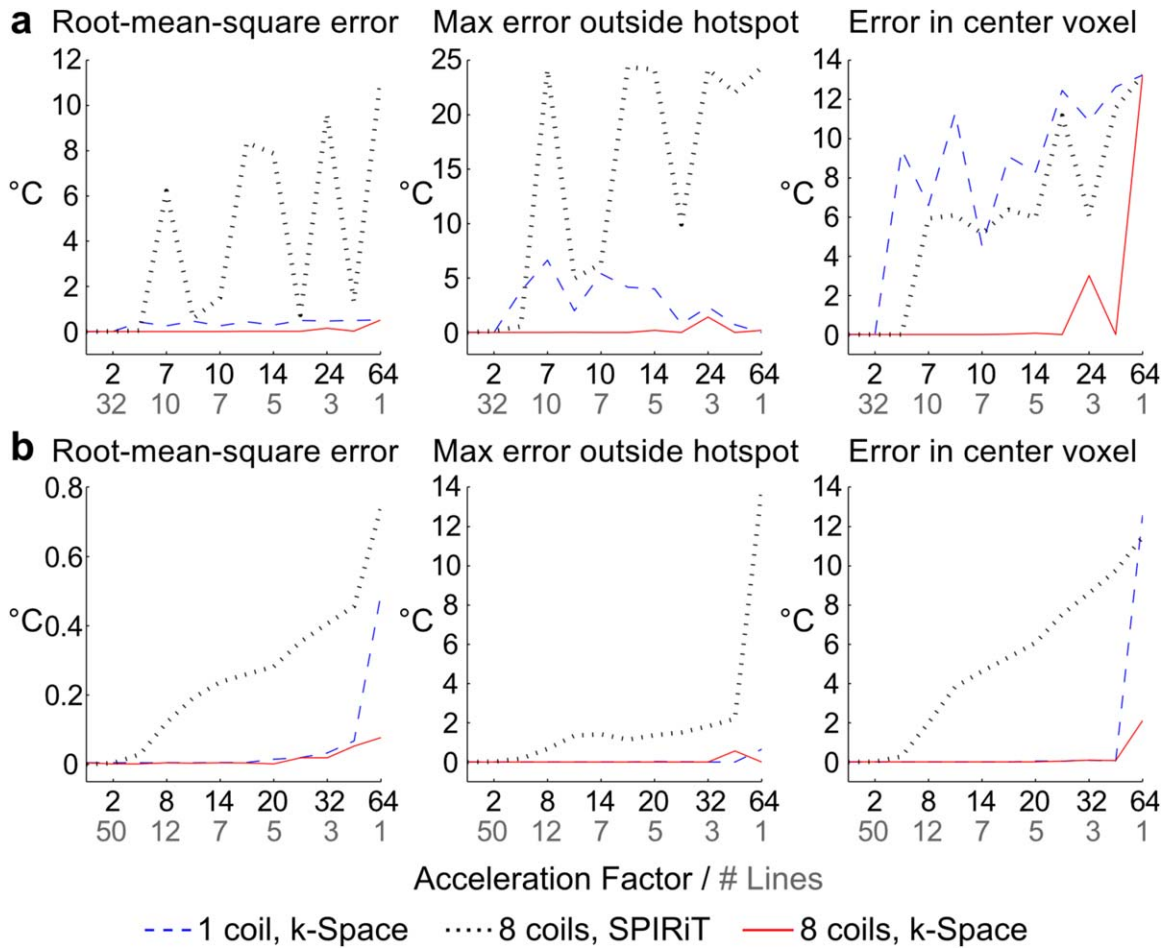
FIG. 2. Multicoil receive simulation. RMS error, maximum error outside the hot spot, and error in the center voxel are plotted for (**a**) 2DFT and (**b**) GA radial trajectories. Black labels along the *x*-axis indicate acceleration factor, and gray labels indicate the corresponding number of readout lines used in the reconstruction. k-Space reconstruction errors are generally lower than SPIRiT errors, and multicoil k-space estimates have lower error than single-coil estimates.

shows that the k-space temperature maps were free from artifacts over the entire course of the experiment, and closely matched the fully-sampled reconstructions. Temperature changes were overestimated in the SPIRiT temperature maps throughout the experiment.

Results from the GA radial scan are shown in Figure 5. As in the 2DFT case, large aliasing artifacts are present in CG and SPIRiT reconstructions, but not in k-space-based reconstructions. At $16\times$ acceleration, SPIRiT-based temperature estimates are consistently lower than the heating estimated from fully-sampled data. The k-space temperature reconstruction algorithm produces heating estimates that closely match the fully-sampled results throughout the experiment.

In Vivo Model Validation

Figure 6 shows the in vivo model validation results. As expected, temperature errors increased with acceleration factor for all reconstruction methods. At high acceleration factors, the CG-reconstructed temperature maps have large errors, which are reduced but not removed using SPIRiT. The k-space method's maps reflect a glob-

ally increased temperature uncertainty resulting from lower SNR, but no significant aliasing artifacts within the brain up to $32\times$ acceleration.

Computation Time

Table 1 shows the computation times for the proposed algorithm, averaged over 10 repeated reconstructions, for one temperature map from simulated and phantom heating data. 2DFT reconstructions used approximately twice as many k-space samples per map as GA radial reconstructions, and required almost twice as much time (15 s vs. 8 s for the same number of iterations). Reconstruction times were significantly longer for simulated data, which were likely due to the lack of noise in the simulations, and a lack of spatial roughness regularization.

DISCUSSION

The proposed k-space-based temperature reconstruction approach was demonstrated in simulations and experiments to produce accurate temperature maps from undersampled k-space data. Temporal step response
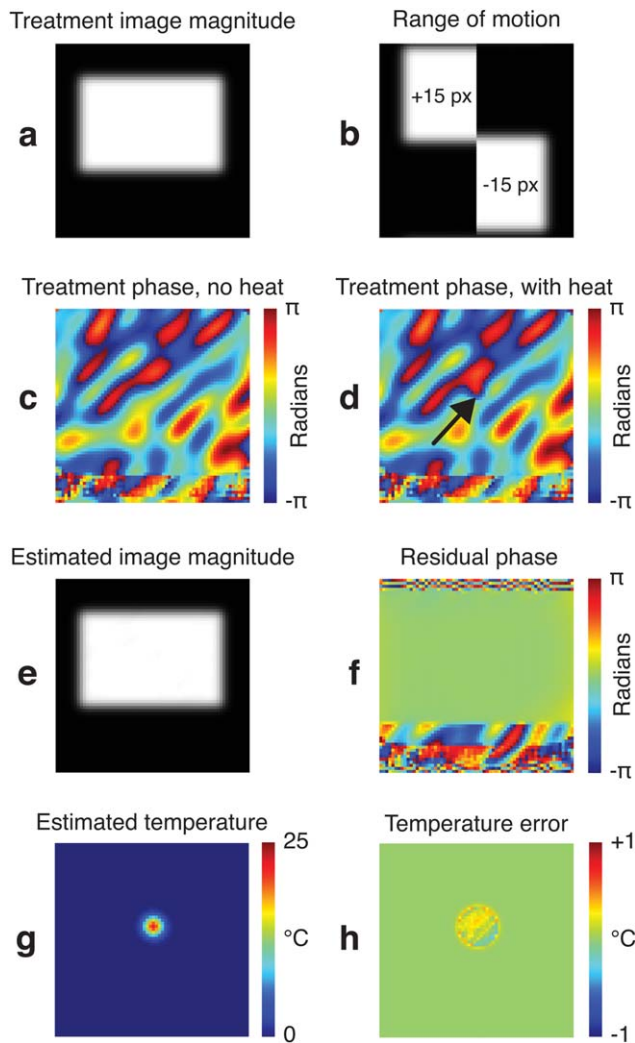
FIG. 3. Motion simulation. **a**: The treatment magnitude image, containing the moving rectangular object. **b**: The first and last images in the baseline library, indicating the range of object motion. **c**: A treatment image phase, with no heat present, contains polynomial and low frequency Fourier components. **d**: The same phase in (c), with the Gaussian hot spot. **e**: The estimated image magnitude, derived from the weighted baseline images. **f**: Residual phase difference between the images in (e) and (a). **g**: The estimated Gaussian-shaped temperature shift. **h**: Temperature map error.

function simulations demonstrated that the method reconstructs 4×-undersampled temperature maps with finer temporal resolution than the TCR method, which uses temporal regularization to suppress undersampling artifacts. Small errors were observed around the edges of the hot spot due to thresholding (RMS error: 0.0047°C; max error: 0.074°C), but undersampling artifacts were not present in the k-space-based temperature reconstructions. Due to their broader temporal point spread function, TCR maps had large errors during rapid temperature changes, with a streaking pattern typical of radial undersampling (RMS error: 0.23°C; max error: 2.98°C). Although increased temporal regularization could have reduced TCR aliasing artifacts, this would

have further decreased its effective temporal resolution. We note that this simulation was designed to compare the response of the two algorithms to large instantaneous temperature rises, which do not occur in practice. However, frame rates of one volume every few seconds are common in thermometry, especially with the desire to increase volumetric coverage. This leads to the possibility that large temperature changes can occur within one to two time frames, and in such cases it is preferable that the reconstructed temperature maps have a temporal resolution that is no coarser than the data frame rate. Future work will apply the proposed algorithm to enable expanded volumetric coverage in MR thermometry, without sacrificing temporal resolution.

Multicoil receive simulations demonstrated that the k-space algorithm benefits from multicoil reception. For 2DFT and GA radial trajectories, k-space temperature estimates from multicoil data had lower error within and outside the hot spot using as few as four (2DFT) and two (GA radial) readout lines. The results suggest that using multiple receive coils may be more advantageous for Cartesian trajectories, although additional experiments will be needed to evaluate this. In both Cartesian and non-Cartesian simulations, low-error temperature reconstructions were achieved at higher levels of acceleration using the k-space method compared to using parallel imaging alone.

A similar pattern was observed in phantom heating experiments. 2DFT and GA radial data were undersampled at 2.5× and 16×, respectively. Results showed that undersampled k-space temperature reconstructions closely matched the fully-sampled temperature maps, and in both experiments the k-space reconstructions were free from aliasing artifacts. In comparison, SPIRiT-based temperature maps suffered from aliasing artifacts and degraded accuracy across the timecourse of the experiments. Unlike the SPIRiT-based temperature reconstructions, the accuracy of the k-space reconstructions was not significantly affected by the relative orientation of the undersampling and coil array dimensions, though it may be more sensitive to relative orientation at higher acceleration factors.

To validate the hybrid k-space signal model and investigate possible temperature errors that could arise in the method, data from a healthy volunteer were collected without heating. Above moderate acceleration factors, large errors became apparent in CG temperature reconstructions. SPIRiT maps also had high error at these factors, although they appeared diminished compared to CG results. Error maps from k-space reconstructions were affected by decreasing SNR, but no significant artifacts appeared until the data were accelerated at 32×. These results suggest that the hybrid k-space signal model accurately captures anatomic phase variations and smooth phase shifts, over a wide range of acceleration factors in vivo. The results of the motion simulation further demonstrated the algorithm's ability to regress background anatomical phase in the presence of motion.

Compared to temporal regularization-based approaches such as TCR, the k-space-based algorithm makes no assumptions on the temporal dynamics of temperature, and was shown in simulations to provide superior
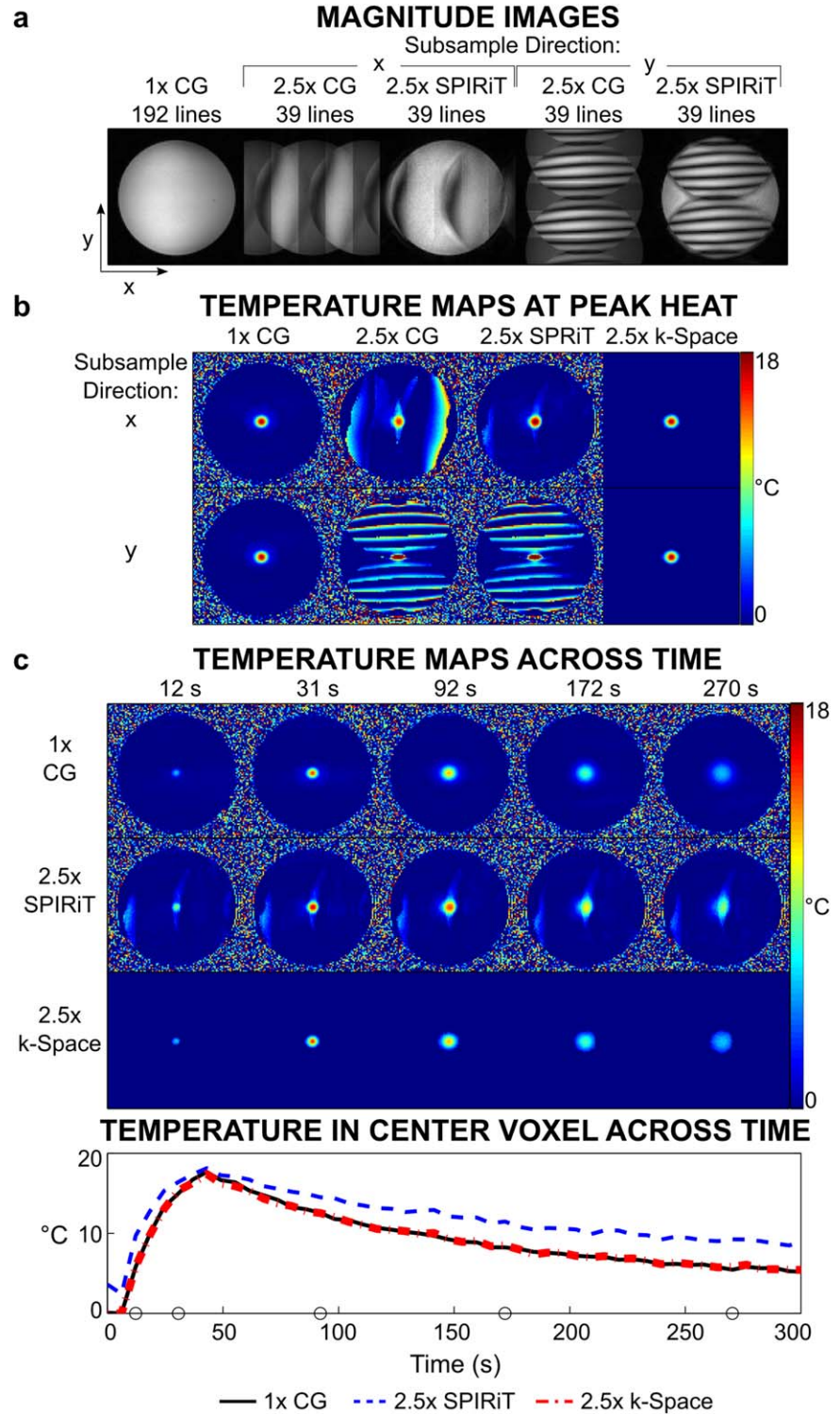
FIG. 4. 2DFT experiment. **a**: Magnitude images reconstructed with full sampling (left) and 2.5× undersampling in the *x*- or *y*-dimensions. **b**: Temperature maps reconstructed at peak from data undersampled in either the *x*- or *y*-dimensions using CG, SPIRiT, and k-space-based methods. **c**: Temperature maps reconstructed along the timecourse of the heating experiment using CG and full sampling (top), SPIRiT-reconstructed images and 2.5× undersampling along the *x*-direction (middle), and the k-space method and 2.5× undersampling along the *x*-direction (bottom). Bottom: Plot of temperature evolution in the central voxel as a function of time for fully-sampled (CG) and 2.5×-undersampled (SPIRiT and k-space-domain) temperature maps. Circles along the *x*-axis indicate times of the displayed temperature maps.

temporal resolution to TCR. The k-space algorithm also does not require k-space undersampling patterns to change between consecutive acquisitions, as was demonstrated by the 2DFT phantom reconstructions, where the accelerated sampling pattern was held fixed for the entire duration of the experiment. However, higher accelerations may be possible with the proposed method if temporal regularization is added to the objective function

in Eq. [2] and an alternating k-space sampling pattern is used.

Although the proposed algorithm expands on the capabilities of hybrid multibaseline and referenceless thermometry (38), it also inherits some of its limitations. One is that the algorithm requires the assumption of focal heating to separate heat-induced phase shift from the polynomial phase shifts. Thus, in its current form the
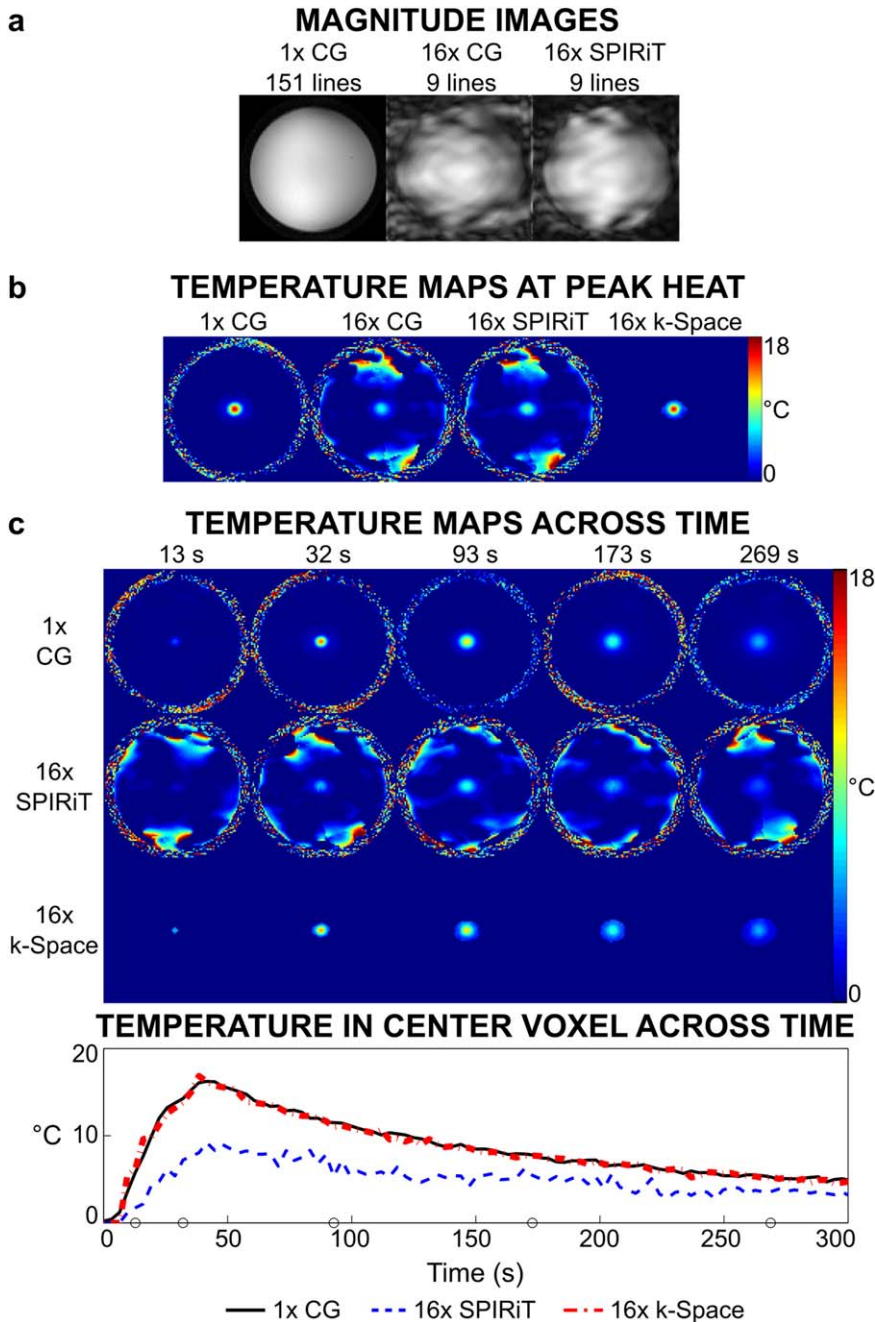
a
MAGNITUDE IMAGES
| 1x CG | 16x CG | 16x SPIRiT |
| 151 lines | 9 lines | 9 lines |

b
TEMPERATURE MAPS AT PEAK HEAT
1x CG   16x CG   16x SPIRiT   16x k-Space

c
TEMPERATURE MAPS ACROSS TIME
13 s   32 s   93 s   173 s   269 s

1x CG

16x SPIRiT

16x k-Space

TEMPERATURE IN CENTER VOXEL ACROSS TIME

—— 1x CG   - - - 16x SPIRiT   -·-·- 16x k-Space

FIG. 5. GA radial experiment. **a**: Magnitude images reconstructed with full sampling (left) and 16× undersampling with CG (middle) and SPIRiT reconstructions (right). **b**: Temperature maps reconstructed at peak heat using fully-sampled CG and 16×-undersampled CG, SPIRiT, and k-space-based models. **c**: Top: Temperature maps reconstructed along the timecourse of the heating experiment with full sampling using CG (top), 16×-undersampling using SPIRiT-reconstructed images (middle), and 16×-undersampling using k-space reconstruction (bottom). Bottom: Plot of temperature evolution in the central voxel as a function of time for fully-sampled (CG) and 16×-undersampled (SPIRiT and k-space-domain) temperature maps. Circles along the x-axis indicate times of the displayed temperature maps.

algorithm may not be suitable for imaging more diffuse heating patterns such as heating caused by RF electric fields generated by the MRI scanner (specific absorption rate [SAR]), which may be well-modeled by polynomials. An extension to those cases would require development of new approaches to the background and heating phase separation problem, which could then be incorporated with the algorithm. If tissue motion occurs in a direction not captured by the baseline library, the method will also become inaccurate. However, if registration information is available to track this motion, it may be possible to reuse previously acquired baseline images in the new orientation, as smooth phase shifts caused by reorientation of the tissue in the magnet could be captured by the polynomial

phase shift. Finally, like the original hybrid thermometry method, the proposed algorithm does not account for the presence of fat in heated voxels. Because fat experiences a negligible frequency shift with temperature, its signal degrades the accuracy of temperature estimates when it is present in a voxel but not accounted for. Although it is common to suppress fat in PRF-shift thermometry acquisitions using spectral-spatial excitations (49), its signal can be used for thermometry based on changes in longitudinal or transverse relaxation rates, or as a temperature-independent phase or frequency reference for PRF-shift thermometry. In those scenarios, multiecho acquisitions can enable separation of water and fat signals. To apply the proposed k-space algorithm to such acquisitions, a
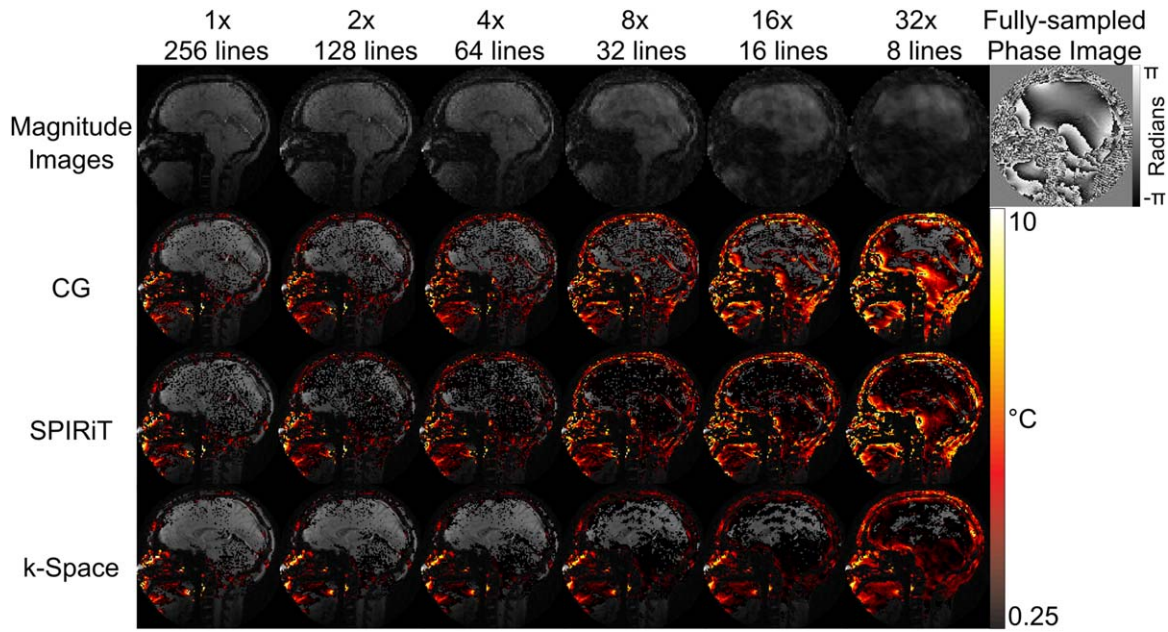
FIG. 6. In vivo model validation (no heating). Top row: Magnitude images reconstructed at different acceleration factors. The phase of one fully-sampled image is shown at the top right. Bottom three rows: Comparison of mean positive temperature errors over 0.25°C for CG, SPIRiT, and k-space temperature reconstructions. Moderate acceleration leads to large temperature errors in the CG and SPIRiT reconstructions, but the k-space reconstructions suffer only an apparent loss in SNR in the brain up to 32× acceleration.

multiecho signal model would need to be developed that comprises both water and fat components, and that solves for a heat-induced frequency shift (rather than a phase shift) in water. Such a model would incorporate previously acquired and separated water and fat baseline images. Extensions of the original hybrid method have been developed that estimate heat-induced frequency changes from multiecho acquisitions (50), and that use fat images as a phase reference for PRF thermometry (51).

For the current implementation of the algorithm, the measured compute times for one frame were on the order of 8–15 s. Although not compatible with real-time clinical use, these times are feasible for retrospective reconstructions that would be useful for preclinical studies (52). Furthermore, the current implementation used only one CPU core, and a multithreaded or GPU-based implementation of the algorithm may yield compute times compatible with real-time use (53). The presented reconstructions also used a nonuniform Fast Fourier Transform algorithm to evaluate multiplications with the **G** matrix, which includes a computationally expensive gridding step (44). This step could be eliminated for Cartesian-sampled data (2DFT and EPI), which are the most commonly used k-space trajectories in thermometry. Finally, initializing the algorithm with a previous solution for the temperature map, baseline weights and polynomial coefficients could help accelerate convergence, particularly when little or no motion is present. As for any reconstruction approach, multislice temperature reconstructions could be parallelized across slices, so the in-plane acceleration enabled by a real-time-compatible extension of the proposed algorithm could be leveraged to increase the number of acquired slices, without sacrificing temporal resolution. Further development of the algorithm to achieve real-time compute times will be the focus of future research efforts.

CONCLUSIONS

Accelerated temperature imaging is important to support current and enable future MRI-guided thermal interventions. We have presented an algorithm for temperature reconstruction by fitting a constrained model directly to k-space data. The proposed algorithm is capable of estimating focal temperature changes from k-space data with high temporal resolution and accuracy, even at high acceleration factors.

APPENDIX

Nonlinear Conjugate Gradient Algorithm for θ Updates

The steps of the nonlinear CG algorithm (42) used to update the heating-induced phase shift θ in step 3 of the algorithm are:

Table 1
Computation Time and Iteration Count

Dataset, acceleration factor	Time (s)	Number of iterations
Simulated phantom, 4×	74.1	Steps 1–5: 6; step 6: 3
2DFT gel phantom, 2.5×	14.6	Steps 1–5: 3; step 6: 3
GA radial gel phantom, 16×	8.2	Steps 1–5: 3; step 6: 3

1. **repeat**
2. Calculate search direction $\boldsymbol{p}$: A column vector $\boldsymbol{g} = \nabla_{\boldsymbol{\theta}}\Psi$ of the first derivatives of the objective function $\Psi(\boldsymbol{\theta})$ in Eq. [4] with respect to the elements of $\boldsymbol{\theta}$ is first calculated as:

$$\boldsymbol{g}^n = \nabla_{\boldsymbol{\theta}}\Psi = \Re\left\{\imath\,\mathrm{diag}\left\{f_j^* e^{-\imath\theta_j^n}\right\}\boldsymbol{G}'\left(\tilde{\boldsymbol{y}} - \boldsymbol{G}\mathrm{diag}\left\{e^{\imath\theta_j^n}\right\}\boldsymbol{f}\right)\right\},$$

[7]

where $\boldsymbol{G}$ is a (nonuniform) DFT matrix. Using the Polack–Ribière conjugate gradient formula, the search direction at iteration n is given by:

$$\boldsymbol{p}^n = \begin{cases} -\boldsymbol{g}^n, & n = 0 \\ -\boldsymbol{g}^n + \dfrac{\langle\boldsymbol{g}^n - \boldsymbol{g}^{n-1}, \boldsymbol{g}^n\rangle}{||\boldsymbol{g}^{n-1}||^2}\boldsymbol{p}^{n-1}, & n \geq 1 \end{cases}$$

[8]

3. Calculate step size α: α is evaluated subject to non-positivity constraints as follows: If $\theta_j^n > \epsilon$ for some threshold ϵ ($\epsilon = \pi/1000$ was used in the present work) and $p_j^n > 0$, then set $p_j^n = 0$ since the search direction will lead to violation of the nonpositivity constraint at that location, for any α. Then, solve

$$\alpha_n = \underset{\alpha}{\mathrm{argmin}}\ \Psi(\boldsymbol{\theta^n} + \alpha\boldsymbol{p}^n)$$

[9]

using a backtracking line search. Next, determine if the α returned by the line search causes violation of the nonpositivity constraint. Let $\boldsymbol{z}^n = \boldsymbol{\theta}^n + \alpha_n\boldsymbol{p}^n$. If $[\boldsymbol{z}^n]_- \neq \boldsymbol{z}^n$, then set

$$\boldsymbol{p}^n = [\boldsymbol{z}^n]_- - \boldsymbol{\theta}^n$$

[10]

and perform another backtracking line search with the updated $\boldsymbol{p}^n$:

$$\alpha_n = \underset{\alpha\in[0,1]}{\mathrm{argmin}}\ \Psi(\boldsymbol{\theta^n} + \alpha\boldsymbol{p}^n)$$

[11]

4. Update $\boldsymbol{\theta}$: $\boldsymbol{\theta}^{n+1} = \boldsymbol{\theta}^n + \alpha\boldsymbol{p}^n$
5. **until** The desired number of iterations is reached.

REFERENCES

1. Kennedy JE, Ter Haar GR, Cranston D. High intensity focused ultrasound: surgery of the future? Br J Radiol 2003;76:590–599.
2. Huber PE, Jenne JW, Rastert R, Simiantonakis I, Sinn HP, Strittmatter HJ, von Fournier D, Wannenmacher MF, Debus J. A new noninvasive approach in breast cancer therapy using magnetic resonance imaging-guided focused ultrasound surgery. Cancer Res 2001;61:8441–8447.
3. Hynynen K, Pomeroy O, Smith DN, Huber PE, McDannold NJ, Kettenbach J, Baum J, Singer S, Jolesz FA. MR Imaging-guided focused ultrasound surgery of fibroadenomas in the breast: a feasibility study1. Radiology 2001;219:176–185.
4. Tempany CMC, Stewart EA, McDannold N, Quade BJ, Jolesz F, Hynynen K. MR imaging-guided focused ultrasound surgery of uterine leiomyomas: a feasibility study. Radiology 2003;226:897–905.
5. McDannold NJ, Clement GT, Black P, Jolesz FA, Hynynen K. Transcranial magnetic resonance imaging – guided focused ultrasound surgery of brain tumors. Neurosurgery 2010;66:323–332.
6. Catane R, Beck A, Inbar Y, Rabin T, Shabshin N, Hengst S, Pfeffer RM, Hanannel A, Dogadkin O, Liberman B. MR-guided focused ultrasound surgery (MRgFUS) for the palliation of pain in patients with bone metastases—preliminary clinical experience. Ann Oncol 2007;18:163–167.
7. Liberman B, Gianfelice D, Inbar Y, Beck A, Rabin T, Shabshin N, Chander G, Hengst S, Pfeffer R, Chechick A. Pain palliation in patients with bone metastases using MR-guided focused ultrasound surgery: a multicenter study. Ann Surg Oncol 2009;16:140–146.
8. Martin E, Jeanmonod D, Morel A, Zadicario E, Werner B. High-intensity focused ultrasound for noninvasive functional neurosurgery. Ann Neurol 2009;66:858–861.
9. Elias WJ, Huss D, Voss T, et al. Pilot study of focused ultrasound thalamotomy for essential tremor. New Engl J Med 2013;369:640–648.
10. Madio DP, Van Gelderen P, DesPres D, Olson AW, De Zwart JA, Fawcett TW, Holbrook NJ, Mandel M, Moonen CTW. On the feasibility of MRI-guided focused ultrasound for local induction of gene expression. J Magn Reson Imaging 1998;8:101–104.
11. de Zwart J, Salomir R, Vimeux F, Klaveness J, Moonen C. On the feasibility of local drug delivery using thermo-sensitive liposomes and MR-guided focused ultrasound. In Proceedings of the 8th Annual Meeting of ISMRM, Sydney, Australia, 2000. p. 3.
12. Hynynen K, McDannold N, Vykhodtseva N, Jolesz F. Noninvasive MR imaging-guided focal opening of the blood-brain barrier in rabbits. Radiology 2001;220:640–646.
13. Reinhard M, Hetzel A, Krüger S, Kretzer S, Talazko J, Ziyeh S, Weber J, Els T. Blood-brain barrier disruption by low-frequency ultrasound. Stroke 2006;37:1546–1548.
14. Köhler MO, Mougenot C, Quesson B, Enholm J, Le Bail B, Laurent C, Moonen CTW, Ehnholm GJ. Volumetric HIFU ablation under 3D guidance of rapid MRI thermometry. Med Phys 2009;36:3521.
15. Mougenot C, Kohler MO, Enholm J, Quesson B, Moonen C. Quantification of near-field heating during volumetric MR-HIFU ablation. Med Phys 2011;38:272–282.
16. Moonen CT, Quesson B, Salomir R, Vimeux FC, de Zwart J, Van Vaals JJ, Grenier N, Palussiere J. Thermal therapies in interventional MR imaging. Focused ultrasound. Neuroimaging Clin N Am 2001;11: 737–747.
17. Yuan J, Mei CS, Panych LP, McDannold NJ, Madore B. Towards fast and accurate temperature mapping with proton resonance frequency-based MR thermometry. Quant Imaging Med Surg 2012;2:21–32.
18. Pruessmann KP, Weiger M, Scheidegger MB, Boesiger P. SENSE: sensitivity encoding for fast MRI. Magn Reson Med 1999;42:952–962.
19. Griswold MA, Jakob PM, Heidemann RM, Nittka M, Jellus V, Wang J, Kiefer B, Haase A. Generalized autocalibrating partially parallel acquisitions (GRAPPA). Magn Reson Med 2002;47:1202–1210.
20. Weidensteiner C, Kerioui N, Quesson B, Denis de Senneville B, Trillaud H, Moonen CTW. Stability of real-time MR temperature mapping in healthy and diseased human liver. J Magn Reson Imaging 2004;19:438–446.
21. Bankson JA, Stafford RJ, Hazle JD. Partially parallel imaging with phase-sensitive data: increased temporal resolution for magnetic resonance temperature imaging. Magn Reson Med 2005;53:658–665.
22. Guo JY, Kholmovski EG, Zhang L, Jeong EK, Parker DL. K-space inherited parallel acquisition (KIPA): application on dynamic magnetic resonance imaging thermometry. Magn Reson Med 2006;24:903–915.
23. Streicher MN, Schafer A, Muller D, et al. Frequency-selective asymmetric spin-echo EPI with parallel imaging for fast internally referenced MR Thermometry. In Proceedings of the 19th Annual Meeting of ISMRM, Montreal, Canada, 2011. p. 529.
24. Mei CS, Panych LP, Yuan J, McDannold NJ, Treat LH, Jing Y, Madore B. Combining two-dimensional spatially selective RF excitation, parallel imaging, and UNFOLD for accelerated MR thermometry imaging. Magn Reson Med 2011;66:112–122.
25. Kohler MO, Tillander M, Syrja A, Nakari R, Ylihautala M. Ultrasound-transparent RF coil design for improved MR thermometry of HIFU therapy. In Proceedings of the 19th Annual Meeting of ISMRM, Montreal, Canada, 2011. p. 1728.
26. Minalga E, Merrill R, Todd N, Parker DL, Hadley JR. A 10-channel RF coil for use in magnetic resonance guided high intensity focused ultrasound for the brain. In Proceedings of the 21st Annual Meeting of ISMRM, Salt Lake City, Utah, USA, 2013. p. 832.
27. Minalga E, Payne A, Merrill R, Todd N, Vijayakumar S, Kholmovski E, Parker DL, Hadley JR. An 11-channel radio frequency phased array coil for magnetic resonance guided high-intensity focused ultrasound of the breast. Magn Reson Med 2013;69:295–302.
28. Lustig M, Donoho D, Pauly JM. Sparse MRI: the application of compressed sensing for rapid MR imaging. Magn Reson Med 2007;58: 1182–1195.

29. Leonard P, Chopra R, Nachman A. Compressed sensing for accelerated MR thermometry in MRI-controlled transurethral ultrasound therapy. In Proceedings of the 20th Annual Meeting of ISMRM, Melbourne, Australia, 2012. p. 2918.

30. Marx M, Butts Pauly K. Use of compressed sensing for acceleration of volumetric MR thermometry. In ISMRM Workshop on Data Sampling & Image Reconstruction, Sedona, Arizona, USA, 2013.

31. Zhao F, Noll DC, Nielsen JF, Fessler JA. Separate magnitude and phase regularization via compressed sensing. IEEE Trans Med Imaging 2012;31:1713–1723.

32. Cao Z, Oh S, Otazo R, Sica CT, Griswold MA, Collins CM. Complex difference constrained compressed sensing reconstruction for accelerated PRF thermometry with application to MRI-induced RF heating. Magn Reson Med 2015;73:1420–1431.

33. Todd N, Adluru G, Payne A, DiBella EVR, Parker DL. Temporally constrained reconstruction applied to MRI temperature data. Magn Reson Med 2009;62:406–419.

34. Todd N, Payne A, Parker DL. Model predictive filtering for improved temporal resolution in MRI temperature imaging. Magn Reson Med 2010;63:1269–1279.

35. Roujol S, Ries M, Quesson B, Moonen CTW, Denis de Senneville B. Real-time MR-thermometry and dosimetry for interventional guidance on abdominal organs. Magn Reson Med 2010;63:1080–1087.

36. Gaur P, Grissom WA. Direct reconstruction of proton resonance frequency-shift temperature maps from k-space data for highly accelerated thermometry. In Proceedings of the 21st Annual Meeting of ISMRM, Salt Lake City, Utah, USA, 2013. p. 1805.

37. Gaur P, Grissom WA. MRI temperature map reconstruction from highly undersampled data. In 13th International Symposium on Therapeutic Ultrasound, Shanghai, People's Republic of China, 2013.

38. Grissom WA, Rieke V, Holbrook AB, Medan Y, Lustig M, Santos J, McConnell MV, Pauly KB. Hybrid referenceless and multibaseline subtraction MR thermometry for monitoring thermal therapies in moving organs thermometry for monitoring thermal therapies in moving organs. Med Phys 2010;37:5014–5026.

39. Rieke V, Instrella R, Rosenberg J, Grissom WA, Werner B, Martin E, Butts Pauly K. Comparison of temperature processing methods for monitoring focused ultrasound ablation in the brain. J Magn Reson Imaging 2013;38:1462–1471.

40. Holbrook AB, Ghanouni P, Santos JM, Medan Y, Pauly KB. In vivo MR acoustic radiation force imaging in the porcine liver. Med Phys 2011;38:5081.

41. Rieke V, Pauly KB. MR thermometry. J Magn Reson Imaging 2008;27:376–390.

42. Qi J, Leahy RM, Hsu C, Farquhar TH, Cherry SR. Fully 3D Bayesian image reconstruction for the ECAT EXACT HR+. IEEE Trans Nuc Sci. 1998;45:1096–1103.

43. Pruessmann KP, Weiger M, Börnert P, Boesiger P. Advances in sensitivity encoding with arbitrary k-space trajectories. Magn Reson Med 2001;46:638–651.

44. Fessler JA, Sutton BP. Nonuniform fast fourier transforms using min-max interpolation. IEEE Trans Signal Process 2003;51:560–574.

45. Sutton BP, Noll DC, Fessler JA. Fast, iterative image reconstruction for MRI in the presence of field inhomogeneities. IEEE Trans Med Imaging 2003;22:178–188.

46. Lustig M, Pauly JM. SPIRiT: iterative self-consistent parallel imaging reconstruction from arbitrary k-space. Magn Reson Med 2010;64:457–471.

47. Wright SM. 2D full wave modeling of sense coil geometry factors at high fields. In Proceedings of the 10th Annual Meeting of ISMRM, Honolulu, Hawaii, USA, 2002. p. 854.

48. Funai AK, Fessler JA, Yeo D, Olafsson VT, Noll DC. Regularized field map estimation in MRI. IEEE Trans Med Imaging 2008;27:1484–1494.

49. de Zwart JA, Vimeux FC, Delalande C, Canioni P, Moonen CT. Fast lipid-suppressed MR temperature mapping with echo-shifted gradient-echo imaging and spectral-spatial excitation. Magn Reson Med 1999;42:53–59.

50. Gaur P, Grissom WA. Comparison of single- and multi-echo PRF-shift thermometry and method for penalized-likelihood multi-echo temperature reconstruction. In Proceedings of the 22nd Annual Meeting of ISMRM, Milan, Italy, 2014. p. 2351.

51. Grissom WA, Hofstetter LW, Rieke V, Medan Y, Butts Pauly K, Davis CE. Hybrid multibaseline and referenceless PRF-shift thermometry using both water and fat images. In Proceedings of the 19th Annual Meeting of ISMRM, Montreal, Canada, 2011. p. 1771.

52. Todd N, Vyas U, de Bever J, Payne A, Parker D. Reconstruction of fully three-dimensional high spatial and temporal resolution MR temperature maps for retrospective applications. Magn Reson Med 2012;67:724–730.

53. Todd N, Prakash J, Odeen H, De Bever J, Payne A, Yalavarthy P, Parker DL. Toward real-time availability of 3D temperature maps created with temporally constrained reconstruction. Magn Reson Med 2013;71:1394–1404.